Explicit dynamic modeling with joint friction and coupling analysis of a 5-DOF hybrid polishing robot

Guo, Feng; Cheng, Gang; Pang, Yusong

DOI
10.1016/j.mechmachtheory.2021.104509

Publication date
2022

Document Version
Final published version

Published in
Mechanism and Machine Theory

Mechanism and Machine Theory 167 (2022) 104509

Contents lists available at ScienceDirect

Mechanism and Machine Theory

journal homepage: www.elsevier.com/locate/mechmt

Explicit dynamic modeling with joint friction and coupling analysis of a 5-DOF hybrid polishing robot

Feng Guo [a], Gang Cheng [a,*], Yusong Pang [b]

[a] School of Mechatronic Engineering, China University of Mining and Technology, Xuzhou 21116, China
[b] Faculty of Mechanical, Maritime and Materials Engineering, Delft University of Technology, Delft 2628, the Netherlands

ARTICLE INFO

Keywords:
Hybrid polishing robot
Newton-Euler method
Explicit dynamic modeling
Joint friction
Inertia coupling

ABSTRACT

Aiming at a 5-DOF hybrid optical mirror polishing robot, the explicit dynamic model considering the joint friction is established and the inertia coupling distribution is studied. Firstly, the kinematics of the manipulator is solved based on closed-loop vector method, and the dynamic model is established with Newton-Euler method based on the force analysis of manipulator components. Secondly, the kinematic parameters of the reference point of the moving platform are selected as the intermediate variables, and the explicit dynamic model of the parallel manipulator is obtained by parameters substitution considering the friction effects of spherical joints, universal joints and ball screws. Finally, on the basis of the dynamic model, the inertia coupling strength evaluation index for active branched-chains is proposed, and the distribution law of the coupling strength in a certain trajectory and workspace is studied. The results show that the inertia coupling strength indices between active branched-chains vary with the manipulator position and are symmetrically distributed in the workspace. This paper provides a theoretical basis for the joint controller design and structural parameter optimization of the polishing robot.

1. Introduction

As a kind of advanced manufacture tool, robots have been widely used in the field of precision machining and play a more and more important role in modern industry [1-3]. With the application of optical free-form surfaces and the requirement of random trajectory processing, the robot used for polishing optical mirrors not only has to drive the grinding system to traverse every point of the mirror surface but also needs to adjust the motion attitude in real time, which makes the drive motors change the motion direction frequently [4, 5]. Therefore, high-precision and high-resolution optical mirrors require high motion performance and accuracy of the polishing robot.

Parallel manipulators with the advantages of high stiffness, high precision and high load capacity have been successfully used in fields with high precision requirements or complex motion trajectories [6, 7]. Meanwhile, the structural optimization, motion control and interference compensation of parallel manipulators have been extensively studied [8, 9]. In the field of polishing processing, Oba et al. proposed a serial-parallel polishing machine for automobile body repair polishing, which can effectively reproduce the polishing action and force of skilled workers [10]. Xu et al. designed a serial-parallel polishing machine for machining the part with free-form surfaces and carried out a series of studies on its performance parameters and experiments [11, 12]. Parallel manipulator is the core component of the hybrid optical mirror processing machine and requires excellent kinematic and dynamic performance, however, the

* Corresponding author.
E-mail addresses: guofengcumt@163.com (F. Guo), chg@cumt.edu.cn (G. Cheng), Y.Pang@tudelft.nl (Y. Pang).

https://doi.org/10.1016/j.mechmachtheory.2021.104509
Received 26 April 2021; Received in revised form 4 July 2021; Accepted 2 August 2021
Available online 16 August 2021

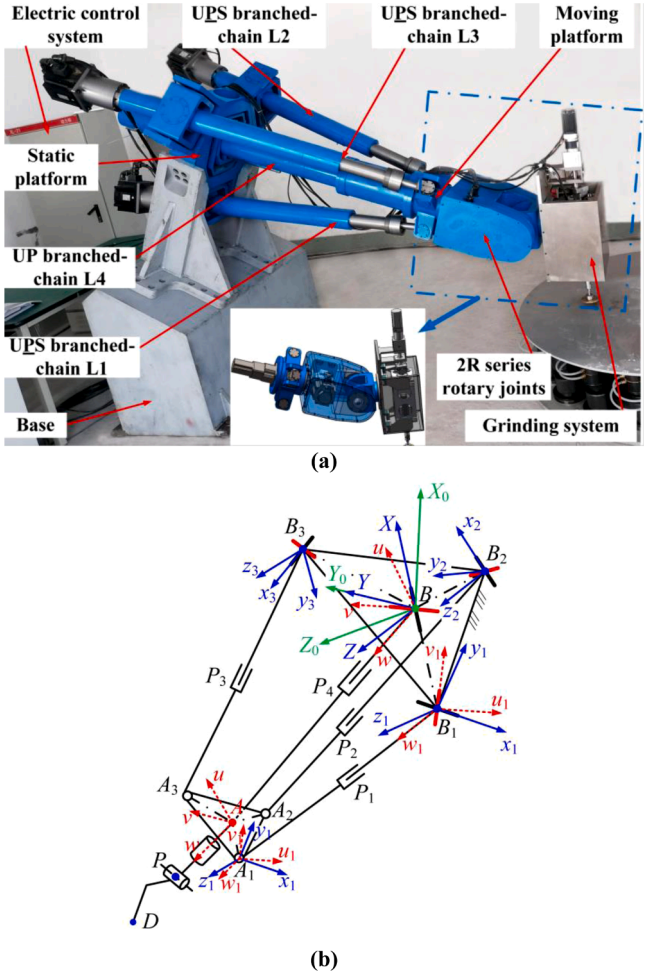

Fig. 1. 5-DOF hybrid optical mirror polishing robot: (a) prototype, (b) topology.

multi-closed-loop structure increases the control difficulty. The kinematics-based control strategies may not meet the robot control requirements, and an effective dynamic model for dynamic control is an important method to improve the manipulator performance. Dynamic modeling methods mainly include Newton-Euler method, Lagrange method, virtual work principle method and Kane method [13-16]. In the dynamic modeling, the effects of the joint clearance, friction, and other factors need to be considered to reflect the actual physical joint effects of the parallel manipulator [17]. Currently, the dynamic model of the parallel manipulator is mostly used to analyze the mechanical properties of manipulators, and there is no uniform requirement for its expression. Although the dynamic modeling based on virtual work principle method and Lagrange method can build an explicit dynamic model of the manipulator, the model solving is tedious when there are many moving components or the joint effects are considered. The physical significance of the dynamic modeling based on Newton-Euler method is clear, and joint forces can be obtained by analyzing each moving component separately, which is extremely beneficial for considering joint effects [18]. Khalil et al. established the explicit dynamic model of Gough-Stewart parallel manipulator with Newton-Euler method, but the inertia matrix, centrifugal force and Coriolis force matrix were not well described and the joint effects were neglected [19]. Shan et al. developed an explicit dynamic model considering the joint friction for 3SPS+1PS parallel manipulator, which can be used directly for dynamic controller design and friction compensation. [20]. In addition, due to the multiple closed-loop and flexible components in parallel manipulators, the coupling between the branched-chains is unavoidable [21]. Scholars mainly focus on the kinematic coupling and the rigid-flexible coupling for parallel manipulators [22, 23], and the study on inertia coupling of the branched-chains of the parallel manipulator is not systematic. For manipulators with high stiffness and high mass of moving components, the coupling effect caused by the branched-chain inertia is more pronounced. Shao et al. studied the matching problem between the motor inertia and branched-chain load for Stewart parallel manipulator [24]; meanwhile, Liu et al. proposed an evaluation index of the coupling property for this parallel manipulator and studied the coupling distribution in the workspace [25]. Li et al. developed a dynamic model of a 5PSS/UPU parallel manipulator based on Newton-Euler method and analyzed the inertia coupling of active branched-chains considering the Coulomb friction effect of the manipulator joints [26]. The large-diameter optical mirror polishing robot requires high precision and has a complex structure and large mass of moving components. Establishing the dynamic model with a clear form and analyzing the coupling properties of the

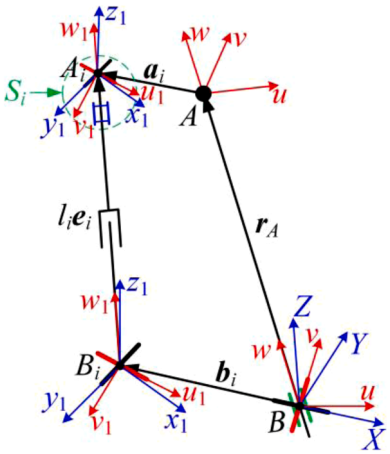

Fig. 2. Diagram of closed-loop vector for UPS branched-chain L*i*.

active branched-chains is of great significance for the controller design and performance improvement.

This paper is organized as follows. In **Section 2**, the structural components and kinematic model of the 5-DOF hybrid polishing robot are described; In **Section 3**, the dynamic model of the polishing robot is developed based on Newton-Euler method considering joint friction; In **Section 4**, the explicit dynamic model with joint friction for the manipulator is obtained by replacing the motion parameters, and the driving forces of active branched-chains are verified by ADAMS; In **Section 5**, on the basis of the explicit dynamic model, the inertia coupling evaluation index of active branched-chains is proposed and the coupling strength distribution in the workspace is analyzed.

2. Description and kinematics analysis of polishing robot

2.1. Description and coordinate systems of polishing robot

The hybrid polishing robot consists of a 3UPS/UP parallel manipulator, 2R series rotary joints and a dual rotor grinding system, and the prototype and topology are shown in Fig. 1. The parallel manipulator comprises a static platform, a moving platform, three UPS active branched-chains (Universal joint - Prismatic pair - Spherical joint) with the same structure and a UP constrained branched-chain (Universal joint - Prismatic pair). Point B_i, the intersection of rotation axes of UPS branched-chain universal joint, is distributed in an equilateral triangle on the static platform with circumcircle radius b. Point A_i, the intersection of rotation axes of the spherical joint, is distributed in an equilateral triangle on the moving platform with circumcircle radius a. Point B, the intersection of rotation axes of UP branched-chain universal joint, coincides with the center of the static platform, and the distribution center of UPS branched-chain spherical joints is marked as A. The prismatic pair of UPS branched-chain is achieved by a ball screw, and the prismatic pair of UP branched-chain is realized by a pair of linear slides. In addition, the static platform of the parallel manipulator is tilted at an angle of thirty degrees to the base bottom to adjust the working position of the polishing robot.

The 2R series rotary joints and dual rotor grinding system follow a simple serial motion. This paper only focuses on the kinematics and dynamics of the parallel manipulator of the polishing robot, and the loads on the parallel manipulator from the 2R series rotary joints and grinding system are considered as external loads. Following the right-hand rule, the coordinate systems of the manipulator are established as follows. The world coordinate system $\{B\text{-}X_0Y_0Z_0\}$ and base coordinate system $\{B\text{-}XYZ\}$ are established at point B, X_0-axis is orthogonal to the base and oriented upward, Z_0-axis is parallel to the base, X-axis coincides with the axis of UP branched-chain universal joint far frame and Z-axis is orthogonal to the static platform plane. The conjoined coordinate system $\{A\text{-}uvw\}$ of UP branched-chain and moving platform is established at point A, v-axis is parallel to the axis of UP branched-chain universal joint near frame and w-axis coincides with the motion axis of UP branched-chain. The reference coordinate system $\{B_i\text{-}x_iy_iz_i\}$ and conjoined coordinate system $\{B_i\text{-}u_iv_iw_i\}$ of UPS branched-chain are established at point B_i, x_i-axis coincides with the axis of UPS branched-chain universal joint far frame, z_i-axis is parallel to Z-axis, v_i-axis coincides with the axis of UPS branched-chain universal joint near frame and w_i-axis coincides with the motion axis of UPS branched-chain. In addition, the reference coordinate system $\{A_i\text{-}x_iy_iz_i\}$ and conjoined coordinate system $\{A_i\text{-}u_iv_iw_i\}$ of the spherical joint are established at point A_i, and the direction of each axis of coordinate systems $\{A_i\text{-}x_iy_iz_i\}$ and $\{A_i\text{-}u_iv_iw_i\}$ is similar to that of coordinate systems $\{B_i\text{-}x_iy_iz_i\}$ and $\{B_i\text{-}u_iv_iw_i\}$. The parallel manipulator of the polishing robot has three independent degrees of freedom, and the serial component of the polishing robot is connected to the moving platform of the parallel manipulator with a slewing bearing, thus the polishing robot can perform five degrees of freedom in its workspace to meet the position and attitude requirements of the dual rotor grinding system.

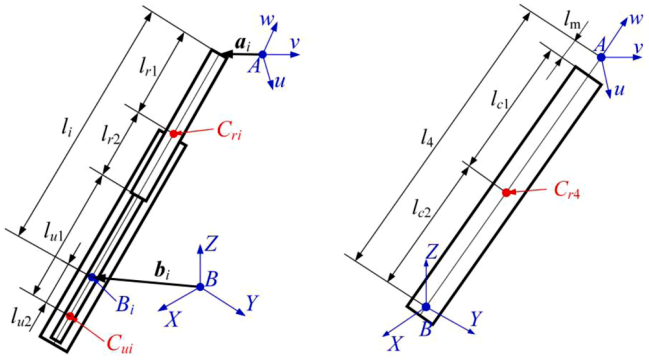

Fig. 3. Structure diagrams of branched-chains: (a) UPS branched-chain, (b) UP branched-chain.

2.2. Kinematic modeling of polishing robot

When the polishing robot is in any position in its workspace, the coordinate matrices of the universal joint center point B_i in the base coordinate system {*B-XYZ*} and the spherical joint center point A_i in the conjoined coordinate system {*A-uvw*} can be expressed as:

$$\begin{bmatrix} \boldsymbol{b}_1 \\ \boldsymbol{b}_2 \\ \boldsymbol{b}_3 \end{bmatrix}^T = \begin{bmatrix} -b & b\sin(\pi/6) & b\sin(\pi/6) \\ 0 & -b\cos(\pi/6) & b\cos(\pi/6) \\ 0 & 0 & 0 \end{bmatrix}, \begin{bmatrix} \boldsymbol{a}_{01} \\ \boldsymbol{a}_{02} \\ \boldsymbol{a}_{03} \end{bmatrix}^T = \begin{bmatrix} -a & a\sin(\pi/6) & a\sin(\pi/6) \\ 0 & -a\cos(\pi/6) & a\cos(\pi/6) \\ 0 & 0 & 0 \end{bmatrix} \tag{1}$$

Combined with Fig. 1(b), the closed-loop vector of UPS branched-chain L*i* (*i*=1, 2, 3) is shown in Fig. 2, and S_i indicates the composite spherical joint, which can be seen as a combination of a universal joint and a rotating joint. In the base coordinate system {*B-XYZ*}, the attitude of the moving platform of the parallel manipulator can be described by Euler angles and the motion equation of the branched-chains can be expressed as:

$$\begin{cases} \boldsymbol{r}_A = \boldsymbol{b}_i + l_i\boldsymbol{e}_i - \boldsymbol{a}_i \\ \boldsymbol{r}_A = l_4\boldsymbol{e}_4 \end{cases} (i = 1, 2, 3) \tag{2}$$

where l_i and $\boldsymbol{e}_i$ are the length and unit vector of the branched-chain L*i* (*i*=1, 2, 3, 4), $\boldsymbol{a}_i = \boldsymbol{R}\boldsymbol{a}_{0i}$ and $\boldsymbol{R}$ is the attitude matrix of the coordinate system {*A-uvw*} relative to the coordinate system {*B-XYZ*}.

The motion parameters of the branched-chains and moving platform can be obtained by deriving and transforming from Eq. (2) and expressed uniformly as the motion parameter mapping of the reference point *A* of the moving platform.

$$\begin{cases} \dot{\boldsymbol{L}} = \boldsymbol{J}\boldsymbol{v}_A \\ \boldsymbol{\omega}_i = \boldsymbol{J}_{\omega i}\boldsymbol{v}_A \\ \boldsymbol{\omega}_{\mathrm{m}} = \boldsymbol{J}_{\omega}\boldsymbol{v}_A \end{cases}, \begin{cases} \ddot{\boldsymbol{L}} = \boldsymbol{J}\dot{\boldsymbol{v}}_A + \dot{\boldsymbol{J}}\boldsymbol{v}_A \\ \dot{\boldsymbol{\omega}}_i = \boldsymbol{J}_{\omega i}\dot{\boldsymbol{v}}_A + \dot{\boldsymbol{J}}_{\omega i}\boldsymbol{v}_A \\ \dot{\boldsymbol{\omega}}_{\mathrm{m}} = \boldsymbol{J}_{\omega}\dot{\boldsymbol{v}}_A + \dot{\boldsymbol{J}}_{\omega}\boldsymbol{v}_A \end{cases}, \ (i = 1, 2, 3) \tag{3}$$

$$\begin{cases} \dot{\boldsymbol{L}} = \begin{bmatrix} \dot{l}_1 & \dot{l}_2 & \dot{l}_3 \end{bmatrix}^T \\ \ddot{\boldsymbol{L}} = \begin{bmatrix} \ddot{l}_1 & \ddot{l}_2 & \ddot{l}_3 \end{bmatrix}^T \end{cases}, \begin{cases} \boldsymbol{J} = \begin{bmatrix} \boldsymbol{e}_1 & \boldsymbol{e}_2 & \boldsymbol{e}_3 \end{bmatrix}^T - \begin{bmatrix} \boldsymbol{a}_1\boldsymbol{e}_1^T\boldsymbol{e}_4 & \boldsymbol{a}_2\boldsymbol{e}_2^T\boldsymbol{e}_4 & \boldsymbol{a}_3\boldsymbol{e}_3^T\boldsymbol{e}_4 \end{bmatrix}^T / l_4 \\ \boldsymbol{J}_{\omega} = \boldsymbol{e}_{4\times}/l_4 \\ \boldsymbol{J}_{\omega i} = \left[\boldsymbol{e}_{i\times} + \left(\boldsymbol{e}_i^T\boldsymbol{a}_i\boldsymbol{E}_3 - \boldsymbol{a}_i\boldsymbol{e}_i^T\right)\boldsymbol{J}_{\omega}\right]/l_i \end{cases} \tag{4}$$

where $\dot{l}_i$ and $\ddot{l}_i$ are the axial velocity and axial acceleration of UPS branched-chain L*i* (*i*=1, 2, 3), $\boldsymbol{\omega}_i$ and $\boldsymbol{\omega}_{\mathrm{m}}$ are the angular velocities of the branched-chain L*i* and moving platform, $\boldsymbol{E}_3$ is the third-order unit matrix, and $\boldsymbol{e}_{i\times}$(*i*=1, 2, 3, 4) is the third-order antisymmetric matrix of $\boldsymbol{e}_i$.

In addition, the axial velocity of UP branched-chain can be expressed as: $\dot{l}_4 = \boldsymbol{J}_4\boldsymbol{v}_A$, and $\boldsymbol{J}_4 = \boldsymbol{e}_4^T$.

Furthermore, the structure diagrams of UPS branched-chain and UP branched-chain are shown in Fig. 3. The velocities and accelerations of the centroid of UPS branched-chain telescopic rod C_{ri}, the centroid of branched-chain cylinder block C_{ui} and the centroid of UP branched-chain C_{r4} are solved as follows:

$$\begin{cases} \boldsymbol{v}_{C_{ri}} = \boldsymbol{J}_{C_{ri}}\boldsymbol{v}_A \\ \boldsymbol{v}_{C_{ui}} = \boldsymbol{J}_{C_{ui}}\boldsymbol{v}_A \\ \boldsymbol{v}_{C_{r4}} = \boldsymbol{J}_{C_{r4}}\boldsymbol{v}_A \end{cases}, \begin{cases} \boldsymbol{a}_{C_{ri}} = \boldsymbol{J}_{C_{ri}}\dot{\boldsymbol{v}}_A + \dot{\boldsymbol{J}}_{C_{ri}}\boldsymbol{v}_A \\ \boldsymbol{a}_{C_{ui}} = \boldsymbol{J}_{C_{ui}}\dot{\boldsymbol{v}}_A + \dot{\boldsymbol{J}}_{C_{ui}}\boldsymbol{v}_A \\ \boldsymbol{a}_{C_{r4}} = \boldsymbol{J}_{C_{r4}}\dot{\boldsymbol{v}}_A + \dot{\boldsymbol{J}}_{C_{r4}}\boldsymbol{v}_A \end{cases}, \ (i = 1, 2, 3) \tag{5}$$

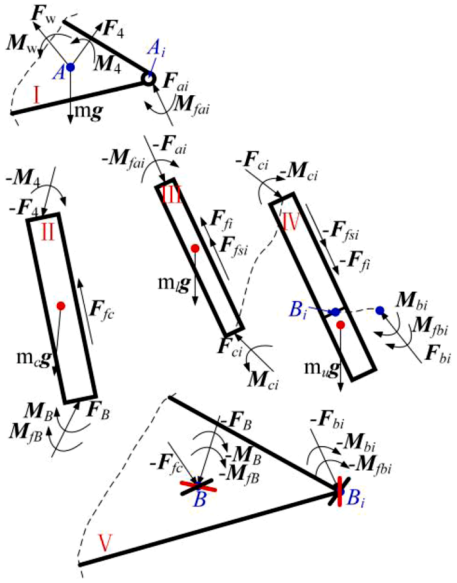

Fig. 4. Force diagram of parallel manipulator: I) moving platform, II) UP branched-chain, III) UPS branched-chain telescopic rod component, IV) UPS branched-chain cylinder block component, V) static platform.

$$\begin{cases} \boldsymbol{J}_{C_{ri}} = \boldsymbol{e}_i \boldsymbol{J}_i + (l_{r1} - l_i)\boldsymbol{e}_{i\times}\boldsymbol{J}_{\omega i} \\ \boldsymbol{J}_{C_{ui}} = l_{u2}\boldsymbol{e}_{i\times}\boldsymbol{J}_{\omega i} \\ \boldsymbol{J}_{C_{r4}} = \boldsymbol{e}_4 \boldsymbol{J}_4 - (1 - (l_{\mathrm{m}} + l_{c1})/l_4)\left(\boldsymbol{E}_3 - \boldsymbol{e}_4 \boldsymbol{e}_4^T\right) \end{cases} \tag{6}$$

where l_{r1} is the length from the centroid of UPS branched-chain telescopic rod to point A_i, l_{u2} is the length from the centroid of branched-chain cylinder block to point B_i, l_{c1} is the length from the centroid of UP branched-chain to its front end, and l_{m} is the length from the front end of UP branched-chain to point A.

3. Dynamic model of polishing robot

To avoid the tedious derivation in dynamic modeling of the parallel manipulator, the dynamic model of parallel manipulator of the polishing robot considering the joint friction effects is established with Newton-Euler method. The force diagram of each component of the parallel manipulator is shown in Fig. 4. Based on Newton-Euler method, the dynamic equations of each manipulator component are established in turn, and the dynamic model of the parallel manipulator was further modeled by eliminating the internal forces between the components. In addition, it is assumed that $\boldsymbol{e}_i^T \boldsymbol{\omega}_i = 0$ and $\boldsymbol{e}_i^T \dot{\boldsymbol{\omega}}_i = 0$ remain valid when the joint friction is considered.

3.1. Dynamic model of moving platform

The moving platform bears the force $\boldsymbol{F}_4$ and the moment $\boldsymbol{M}_4$ of UP branched-chain, the gravity $\mathrm{m}\boldsymbol{g}$, the force of UPS branched-chain $\boldsymbol{F}_{ai}$, the friction moment of spherical joint $\boldsymbol{M}_{fai}$, and the external force and the external moment are denoted as $\boldsymbol{F}_{\mathrm{w}}$ and $\boldsymbol{M}_{\mathrm{w}}$. According to Newton-Euler equation, the dynamic model of the moving platform is as follows:

$$\sum_{i=1}^{3} \boldsymbol{F}_{ai} + \boldsymbol{F}_4 + \mathrm{m}\boldsymbol{g} + \boldsymbol{F}_{\mathrm{w}} = \mathbf{m}\dot{\boldsymbol{v}}_A \tag{7}$$

$$\sum_{i=1}^{3} \boldsymbol{a}_i \times \boldsymbol{F}_{ai} + \sum_{i=1}^{3} \boldsymbol{M}_{fai} + \boldsymbol{M}_4 + \boldsymbol{M}_{\mathrm{w}} = {}^B\boldsymbol{I}_m \dot{\boldsymbol{\omega}}_{\mathrm{m}} + \boldsymbol{\omega}_{\mathrm{m}} \times \left({}^B\boldsymbol{I}_m \boldsymbol{\omega}_{\mathrm{m}}\right) \tag{8}$$

where ${}^B\boldsymbol{I}_{\mathrm{m}}$ is the inertia matrix of the moving platform in the base coordinate system $\{B\text{-}XYZ\}$, ${}^B\boldsymbol{I}_m = \boldsymbol{R}\boldsymbol{I}_m\boldsymbol{R}^T$, and $\boldsymbol{I}_{\mathrm{m}}$ is the inertia matrix of the moving platform in the conjoined coordinate system $\{A\text{-}uvw\}$.

3.2. Dynamic model of UP branched-chain

The UP branched-chain bears the reaction force $\boldsymbol{F}_4$ and reaction moment $\boldsymbol{M}_4$ of the moving platform, the gravity $\mathrm{m}_c\boldsymbol{g}$, the constrained force of the universal joint $\boldsymbol{F}_B$ and the constrained moment of the universal joint $\boldsymbol{M}_B$, the friction force of UP branched-chain

linear slides $\boldsymbol{F}_{fc}$ and the friction moment of UP branched-chain universal joint $\boldsymbol{M}_{fB}$. According to Newton-Euler equation, the dynamic model of UP branched-chain is as follows:

$$\boldsymbol{F}_B + \mathrm{m}_c\boldsymbol{g} + \boldsymbol{F}_{fc} - \boldsymbol{F}_4 = \mathrm{m}_c\boldsymbol{a}_{Cr4} \tag{9}$$

$$l_{c1}(\boldsymbol{e}_4 \times -\boldsymbol{F}_4) + l_{c2}(-\boldsymbol{e}_4 \times \boldsymbol{F}_B) + \boldsymbol{M}_B - \boldsymbol{M}_4 + \boldsymbol{M}_{fB} = {}^B\boldsymbol{I}_c\dot{\boldsymbol{\omega}}_m + \boldsymbol{\omega}_m \times \left({}^B\boldsymbol{I}_c\boldsymbol{\omega}_m\right) \tag{10}$$

where l_{c2} is the length from the centroid of UP branched-chain to point B, ${}^B\boldsymbol{I}_c$ is the inertia matrix of UP branched-chain in the base coordinate system {B-XYZ}, ${}^B\boldsymbol{I}_c = \boldsymbol{R}\boldsymbol{I}_c\boldsymbol{R}^T$, and $\boldsymbol{I}_c$ is the inertia matrix of UP branched-chain in the conjoined coordinate system {A-uvw}.

3.3. Dynamic model of UPS branched-chain

During the optical mirror polishing operation, the motion of each component of UPS branched-chain is not perfectly consistent. The UPS branched-chain can be divided into three components: the branched-chain telescopic rod component, the branched-chain cylinder block component and the branched-chain driving component. The motion state of each component can be expressed as follows:

1) The branched-chain telescopic rod component comprises the branched-chain telescopic rod, the screw nut and the spherical joint, and has a generally rigid motion.
2) The branched-chain cylinder block component comprises the branched-chain cylinder block and the servo motor, and rotates around the point B_i.
3) The branched-chain driving component comprises the servo motor rotor, the coupling and the ball screw, and has a spin motion in addition to the rotation around a fixed point.

In the dynamic modeling of the parallel manipulator, the spin motion of the branched-chain driving component is analyzed separately, and its fixed-point rotation is incorporated into the branched-chain cylinder block component.

3.3.1. Dynamic model of branched-chain telescopic rod component

UPS branched-chain telescopic rod component bears the reaction force of the moving platform $\boldsymbol{F}_{ai}$, the friction moment of the spherical joint $\boldsymbol{M}_{fai}$, the gravity $\mathrm{m}_l\boldsymbol{g}$, the restraint moment of the branched-chain cylinder block component $\boldsymbol{M}_{ci}$ and the friction force $\boldsymbol{F}_{fi}$, the force of the ball screw $\boldsymbol{F}_{ci}$, and the sliding friction force $\boldsymbol{F}_{fsi}$. According to Newton-Euler equation, the dynamic model of the branched-chain telescopic rod component is as follows:

$$\boldsymbol{F}_{ci} - \boldsymbol{F}_{ai} + \mathrm{m}_l\boldsymbol{g} + \boldsymbol{F}_{fi} + \boldsymbol{F}_{fsi} = \mathrm{m}_l\boldsymbol{a}_{Cri} \tag{11}$$

$$l_{r1}(\boldsymbol{e}_i \times -\boldsymbol{F}_{ai}) + l_{r2}(-\boldsymbol{e}_i \times \boldsymbol{F}_{ci}) + \boldsymbol{M}_{ci} - \boldsymbol{M}_{fai} = {}^B\boldsymbol{I}_{li}\dot{\boldsymbol{\omega}}_i + \boldsymbol{\omega}_i \times \left({}^B\boldsymbol{I}_{li}\boldsymbol{\omega}_i\right) \tag{12}$$

where l_{r2} is the length from the action point of the telescopic rod component and the cylinder block component to the centroid of the telescopic rod component, $l_r = l_{r1} + l_{r2}$ and represents the generalized length of the telescopic rod component, ${}^B\boldsymbol{I}_{li}$ is the inertia matrix of the branched-chain telescopic rod component in the base coordinate system {B-XYZ}, ${}^B\boldsymbol{I}_{li} = \boldsymbol{R}_{li}\boldsymbol{I}_{li}\boldsymbol{R}_{li}{}^T$ and $\boldsymbol{I}_{li}$ is the inertia matrix of the telescopic rod component in the conjoined coordinate system {B_i-$u_iv_iw_i$}, $\boldsymbol{R}_{li}$ is the attitude matrix of the conjoined coordinate system {B_i-$u_iv_iw_i$} relative to the base coordinate system {B-XYZ}.

3.3.2. Dynamic model of branched-chain cylinder block component

UPS branched-chain cylinder block component (containing the branched-chain driving component) bears the reaction force $\boldsymbol{F}_{ci}$ and reaction moment $\boldsymbol{M}_{ci}$ of the telescopic rod component, the friction force $\boldsymbol{F}_{fi}$, the sliding friction force $\boldsymbol{F}_{fsi}$, the force $\boldsymbol{F}_{bi}$ and moment $\boldsymbol{M}_{bi}$ of universal joint, the friction moment of the universal joint $\boldsymbol{M}_{fbi}$, and the gravity $\mathrm{m}_u\boldsymbol{g}$. According to Newton-Euler equation, the dynamic model of the branched-chain cylinder block component is as follows:

$$\boldsymbol{F}_{bi} - \boldsymbol{F}_{ci} + \mathrm{m}_u\boldsymbol{g} - \boldsymbol{F}_{fi} - \boldsymbol{F}_{fsi} = \mathrm{m}_u\boldsymbol{a}_{Cui} \tag{13}$$

$$l_{u1}(\boldsymbol{e}_i \times -\boldsymbol{F}_{ci}) + l_{u2}(\boldsymbol{e}_i \times \boldsymbol{F}_{bi}) + \boldsymbol{M}_{bi} - \boldsymbol{M}_{ci} + \boldsymbol{M}_{fbi} = {}^B\boldsymbol{I}_{ui}\dot{\boldsymbol{\omega}}_i + \boldsymbol{\omega}_i \times \left({}^B\boldsymbol{I}_{ui}\boldsymbol{\omega}_i\right) \tag{14}$$

where l_{u1} indicates the length from the action point of the cylinder block component and telescopic rod component to the centroid of the cylinder block component, l_u is the length from the action point of the cylinder block component and telescopic rod component to point B_i and $l_u = l_{u1} - l_{u2}$, ${}^B\boldsymbol{I}_{ui}$ is the inertia matrix of the branched-chain cylinder block component in the base coordinate system {B-XYZ}, ${}^B\boldsymbol{I}_{ui} = \boldsymbol{R}_{li}\boldsymbol{I}_{ui}\boldsymbol{R}_{li}^T$ and $\boldsymbol{I}_{ui}$ is the inertia matrix of the cylinder block component in the conjoined coordinate system {B_i-$u_iv_iw_i$}.

3.3.3. Dynamic model of branched-chain driving component

The inertia moment of the UPS branched-chain driving component is recorded as $\boldsymbol{M}_{si}$, and the dynamic model can be expressed as follows:

$$\boldsymbol{M}_{si} = {}^{B}\boldsymbol{I}_{mi}\dot{\boldsymbol{\omega}}_{mi} + \boldsymbol{\omega}_{mi} \times \left({}^{B}\boldsymbol{I}_{mi}\boldsymbol{\omega}_{mi}\right) \tag{15}$$

where ${}^{B}\boldsymbol{I}_{mi}$ is the inertia matrix of the branched-chain driving component in the base coordinate system {*B-XYZ*}, ${}^{B}\boldsymbol{I}_{mi} = \boldsymbol{R}_{li}\boldsymbol{I}_{mi}\boldsymbol{R}_{li}{}^{T}$ and $\boldsymbol{I}_{mi}$ is the inertia matrix of the branched-chain driving component in the conjoined coordinate system {B_i-$u_iv_iw_i$}. $\omega_{mi} = 2\pi\dot{l}_i/p$ and indicates the angular velocity of the driving component, p is the lead of the ball screw.

3.4. Dynamic model of parallel manipulator of polishing robot

The driving force of UPS branched-chain is noted as F_i. The force $\boldsymbol{F}_{ci}$ acting on the telescopic rod component can be divided into the driving force $F_i\boldsymbol{e}_i$ along the axis of UPS branched-chain and the constrained force $\boldsymbol{F}_{ci}^{\mathrm{n}}$ perpendicular to UPS branched-chain.

According to Eqs. (6), (13) and (14), we can obtain:

$$\begin{aligned}\boldsymbol{M}_{ci} = {} & -l_{u2}m_u\boldsymbol{e}_i \times \boldsymbol{g} - \left(l_i - l_r\right)\left(\boldsymbol{e}_i \times \boldsymbol{F}_{ci}{}^{\mathrm{n}}\right) - l_{u2}^2 m_u\dot{\boldsymbol{\omega}}_i - {}^{B}\boldsymbol{I}_{ui}\dot{\boldsymbol{\omega}}_i \\ & -\boldsymbol{\omega}_i \times \left({}^{B}\boldsymbol{I}_{ui}\boldsymbol{\omega}_i\right) + \boldsymbol{M}_{bi} + \boldsymbol{M}_{fbi}\end{aligned} \tag{16}$$

The force $\boldsymbol{F}_{ai}$ can be divided into the force $\boldsymbol{F}_{ai}^{\mathrm{e}}$ along the axis of UPS branched-chain and the constrained force $\boldsymbol{F}_{ai}^{\mathrm{n}}$ perpendicular to UPS branched-chain. Combining Eqs. (5) and (6), Eq. (11) can be converted to:

$$\begin{aligned}\boldsymbol{F}_{ai}^{\mathrm{e}} + \boldsymbol{F}_{ai}^{\mathrm{n}} - \boldsymbol{F}_{ci}^{\mathrm{n}} = {} & F_i\boldsymbol{e}_i - \mathrm{m}_l\{(l_i - l_{r1})[\dot{\boldsymbol{\omega}}_i \times \boldsymbol{e}_i + \boldsymbol{\omega}_i \times (\boldsymbol{\omega}_i \times \boldsymbol{e}_i)] \\ & + \ddot{l}_i\boldsymbol{e}_i + 2\dot{l}_i\boldsymbol{\omega}_i \times \boldsymbol{e}_i\} + \mathrm{m}_l\boldsymbol{g} + \boldsymbol{F}_{fi} + \boldsymbol{F}_{fsi}\end{aligned} \tag{17}$$

Both sides of Eq. (17) are dot-multiplied or cross-multiplied twice by $\boldsymbol{e}_i$, and we can obtain:

$$\boldsymbol{F}_{ai}^{\mathrm{e}} = F_i\boldsymbol{e}_i - \mathrm{m}_l(l_i - l_{r1})\boldsymbol{\omega}_i \times (\boldsymbol{\omega}_i \times \boldsymbol{e}_i) - \mathrm{m}_l\ddot{l}_i\boldsymbol{e}_i + \mathrm{m}_l\boldsymbol{e}_i\boldsymbol{e}_i^{T}\boldsymbol{g} + \boldsymbol{F}_{fi} + \boldsymbol{F}_{fsi} \tag{18}$$

$$\boldsymbol{F}_{ci}^{\mathrm{n}} = \boldsymbol{F}_{ai}^{\mathrm{n}} - \mathrm{m}_l(l_i - l_{r1})\boldsymbol{e}_i \times \dot{\boldsymbol{\omega}}_i - 2\mathrm{m}_l\dot{l}_i\boldsymbol{e}_i \times \boldsymbol{\omega}_i + \mathrm{m}_l\boldsymbol{e}_i \times (\boldsymbol{e}_i \times \boldsymbol{g}) \tag{19}$$

Substituting $\boldsymbol{F}_{ai}$ and $\boldsymbol{F}_{ci}$ into Eq. (12), and cross-multiplying $\boldsymbol{e}_i$ twice, we can obtain:

$$l_{r1}\boldsymbol{F}_{ai}^{\mathrm{n}} = \boldsymbol{e}_i \times \left({}^{B}\boldsymbol{I}_{li}\dot{\boldsymbol{\omega}}_i\right) + \boldsymbol{e}_i^{T}\left({}^{B}\boldsymbol{I}_{li}\boldsymbol{\omega}_i\right)\boldsymbol{\omega}_i - \boldsymbol{e}_i \times \left(\boldsymbol{M}_{ci} - \boldsymbol{M}_{fai}\right) - l_{r2}\boldsymbol{F}_{ci}^{\mathrm{n}} \tag{20}$$

Combining Eqs. (16) and (19), Eq. (20) can be rewritten as:

$$\begin{aligned}\boldsymbol{F}_{ai}^{\mathrm{n}} = {} & \frac{1}{l_i}\boldsymbol{e}_i \times \left[\left({}^{B}\boldsymbol{I}_{li} + {}^{B}\boldsymbol{I}_{ui}\right)\dot{\boldsymbol{\omega}}_i\right] + \frac{1}{l_i}\boldsymbol{e}_i^{T}\left[\left({}^{B}\boldsymbol{I}_{li} + {}^{B}\boldsymbol{I}_{ui}\right)\boldsymbol{\omega}_i\right]\boldsymbol{\omega}_i \\ & + \frac{2}{l_i}\left(l_i - l_{r1}\right)\mathrm{m}_l\dot{l}_i\boldsymbol{e}_i \times \boldsymbol{\omega}_i + \frac{1}{l_i}\left[l_{u2}m_u - (l_i - l_{r1})\mathrm{m}_l\right]\boldsymbol{e}_i \times (\boldsymbol{e}_i \times \boldsymbol{g}) \\ & + \frac{1}{l_i}\left[(l_i - l_{r1})^2\mathrm{m}_l + l_{u2}^2 m_u\right]\boldsymbol{e}_i \times \dot{\boldsymbol{\omega}}_i - \frac{1}{l_i}\boldsymbol{e}_i \times \left(\boldsymbol{M}_{fbi} - \boldsymbol{M}_{fai}\right)\end{aligned} \tag{21}$$

Eqs. (7), (8), (18) and (21) constitute the entire dynamic model of the polishing robot parallel manipulator considering the joint friction, which can be used to analyze the forces on each component of the parallel manipulator.

4. Explicit dynamic model and simulation

4.1. Explicit dynamic model of polishing robot

The dynamic model obtained in **Section 3** cannot be directly used to design the robot dynamic controller or to analyze the coupling property of the manipulator. Furthermore, in order to obtain the dynamic model of the parallel manipulator with an explicit form, the motion parameters in the dynamic model need to be expressed as the correlation function of the motion parameters of point *A*.

Based on the kinematic analysis and combined with Eqs. (18) and (21), we can obtain:

$$\boldsymbol{F}_{ai}^{\mathrm{e}} - F_i\boldsymbol{e}_i = -\mathrm{m}_l\boldsymbol{e}_i\boldsymbol{J}_i\dot{\boldsymbol{v}}_A + \left[\mathrm{m}_l(l_i - l_{r1})\boldsymbol{e}_i\boldsymbol{v}_A^{T}\boldsymbol{J}_{\omega i}^2 - \mathrm{m}_l\boldsymbol{e}_i\dot{\boldsymbol{J}}_i\right]\boldsymbol{v}_A + \mathrm{m}_l\boldsymbol{e}_i\boldsymbol{e}_i^{T}\boldsymbol{g} + \boldsymbol{F}_{fi} + \boldsymbol{F}_{fsi} \tag{22}$$

$$\begin{aligned}\boldsymbol{F}_{ai}^{\mathrm{n}} = {} & \frac{1}{l_i}\left\{\left({}^{B}\boldsymbol{I}_{li} + {}^{B}\boldsymbol{I}_{ui}\right)\boldsymbol{e}_{i\times}\boldsymbol{J}_{\omega i} + \left[(l_i - l_{r1})^2\mathrm{m}_l + l_{u2}^2 m_u\right]\boldsymbol{e}_{i\times}\boldsymbol{J}_{\omega i}\right\}\dot{\boldsymbol{v}}_A + \frac{1}{l_i}\left\{\left({}^{B}\boldsymbol{I}_{li} + {}^{B}\boldsymbol{I}_{ui}\right)\boldsymbol{e}_{i\times}\dot{\boldsymbol{J}}_{\omega i}\right. \\ & \left. + \left[(l_i - l_{r1})^2\mathrm{m}_l + l_{u2}^2 m_u\right]\boldsymbol{e}_{i\times}\dot{\boldsymbol{J}}_{\omega i} + \boldsymbol{J}_{\omega i}\boldsymbol{v}_A\boldsymbol{e}_i^{T}\left({}^{B}\boldsymbol{I}_{li} + {}^{B}\boldsymbol{I}_{ui}\right)\boldsymbol{J}_{\omega i} + 2\left(l_i - l_{r1}\right)\mathrm{m}_l\boldsymbol{J}_i\boldsymbol{v}_A\boldsymbol{e}_{i\times}\boldsymbol{J}_{\omega i}\right\}\boldsymbol{v}_A \\ & + \frac{1}{l_i}\left[l_{u2}m_u - (l_i - l_{r1})\mathrm{m}_l\right]\boldsymbol{e}_{i\times}^2\boldsymbol{g} - \frac{1}{l_i}\boldsymbol{e}_{i\times}\left(\boldsymbol{M}_{fbi} - \boldsymbol{M}_{fai}\right)\end{aligned} \tag{23}$$

Then, the dynamic model of UPS branched-chain L*i* (*i*=1, 2, 3) can be rewritten as:

$$\boldsymbol{M}_i\dot{\boldsymbol{v}}_A+\boldsymbol{C}_i\boldsymbol{v}_A+\boldsymbol{G}_i+\boldsymbol{\tau}_{fi}=\boldsymbol{\tau}_i \tag{24}$$

$$\begin{cases}\boldsymbol{M}_i=\mathrm{m}_l\boldsymbol{e}_i\boldsymbol{J}_i-(1/l_i)\{\left({}^B\boldsymbol{I}_{li}+{}^B\boldsymbol{I}_{ui}\right)\boldsymbol{e}_{i\times}\boldsymbol{J}_{\omega_i}+\left[(l_i-l_{r1})^2\mathrm{m}_l+l_{u2}^2m_u\right]\boldsymbol{e}_{i\times}\boldsymbol{J}_{\omega_i}\}\\ \boldsymbol{C}_i=-\left[\mathrm{m}_l(l_i-l_{r1})\boldsymbol{e}_i\boldsymbol{v}_A^T\boldsymbol{J}_{\omega i}^2-\mathrm{m}_l\boldsymbol{e}_i\dot{\boldsymbol{J}}_i\right]-(1/l_i)\{\left({}^B\boldsymbol{I}_{li}+{}^B\boldsymbol{I}_{ui}\right)\boldsymbol{e}_{i\times}\dot{\boldsymbol{J}}_{\omega i}+\left[(l_i-l_{r1})^2\mathrm{m}_l+l_{u2}^2m_u\right]\boldsymbol{e}_{i\times}\dot{\boldsymbol{J}}_{\omega i}\\ \quad+\boldsymbol{J}_{\omega i}\boldsymbol{v}_A\boldsymbol{e}_i^T\left({}^B\boldsymbol{I}_{li}+{}^B\boldsymbol{I}_{ui}\right)\boldsymbol{J}_{\omega i}+2\left(l_i-l_{r1}\right)\mathrm{m}_l\boldsymbol{J}_i\boldsymbol{v}_A\boldsymbol{e}_{i\times}\boldsymbol{J}_{\omega i}\}\\ \boldsymbol{G}_i=-(1/l_i)[l_{u2}m_u-(l_i-l_{r1})\mathrm{m}_l]\boldsymbol{e}_{i\times}^2\boldsymbol{g}-\mathrm{m}_l\boldsymbol{e}_i\boldsymbol{e}_i^T\boldsymbol{g}\\ \boldsymbol{\tau}_{fi}=(1/l_i)\boldsymbol{e}_{i\times}\left(\boldsymbol{M}_{fbi}-\boldsymbol{M}_{fai}\right)-\boldsymbol{F}_{fi}-\boldsymbol{F}_{fsi}\\ \boldsymbol{\tau}_i=-\boldsymbol{F}_{ai}+F_i\boldsymbol{e}_i\end{cases}$$

The UP branched-chain of the polishing robot is fixedly connected to the moving platform and the forces on the static platform can be neglected. Substituting the motion parameters into Eqs. (8) and (10), the dynamic model of UP branched-chain and moving platform can be rewritten as:

$$\boldsymbol{M}_{\mathrm{m}}\dot{\boldsymbol{v}}_A+\boldsymbol{C}_{\mathrm{m}}\boldsymbol{v}_A+\boldsymbol{G}_{\mathrm{m}}+\boldsymbol{\tau}_{f\mathrm{m}}+\boldsymbol{E}_{\mathrm{m}}=\boldsymbol{\tau}_{\mathrm{m}} \tag{25}$$

$$\begin{cases}\boldsymbol{M}_{\mathrm{m}}=\boldsymbol{e}_{4\times}\left({}^B\boldsymbol{I}_m+{}^B\boldsymbol{I}_c\right)\boldsymbol{J}_\omega+(l_4-l_{\mathrm{m}})\mathbf{m}\boldsymbol{e}_{4\times}^2+l_{c2}\mathrm{m}_c\boldsymbol{e}_{4\times}^2\boldsymbol{J}_{C_{r4}}\\ \boldsymbol{C}_{\mathrm{m}}=\boldsymbol{e}_{4\times}\left({}^B\boldsymbol{I}_m+{}^B\boldsymbol{I}_c\right)\dot{\boldsymbol{J}}_\omega+\boldsymbol{e}_{4\times}(\boldsymbol{J}_\omega\boldsymbol{v}_A)_\times\left({}^B\boldsymbol{I}_m+{}^B\boldsymbol{I}_c\right)\boldsymbol{J}_\omega+l_{c2}\mathrm{m}_c\boldsymbol{e}_{4\times}^2\dot{\boldsymbol{J}}_{C_{r4}}\\ \boldsymbol{G}_{\mathrm{m}}=-(l_4-l_{\mathrm{m}})\mathrm{m}\boldsymbol{e}_{4\times}^2\boldsymbol{g}-l_{c2}\mathrm{m}_c\boldsymbol{e}_{4\times}^2\boldsymbol{g}\\ \boldsymbol{\tau}_{f\mathrm{m}}=-\boldsymbol{e}_{4\times}\sum_{i=1}^{3}\boldsymbol{M}_{fai}-\boldsymbol{e}_{4\times}\boldsymbol{M}_{fB}\\ \boldsymbol{E}_{\mathrm{m}}=-(l_4-l_{\mathrm{m}})\boldsymbol{e}_{4\times}^2\boldsymbol{F}_{\mathrm{w}}-\boldsymbol{e}_{4\times}\boldsymbol{M}_{\mathrm{w}}\\ \boldsymbol{\tau}_{\mathrm{m}}=\sum_{i=1}^{3}\left(\boldsymbol{e}_{4\times}\boldsymbol{a}_{i\times}+(l_4-l_{\mathrm{m}})\boldsymbol{e}_{4\times}^2\right)\boldsymbol{F}_{ai}\end{cases}$$

Besides, the inertia matrix of the spin motion of UPS branched-chain driving component can be expressed as:

$$M_{si}=\left(\frac{2\pi}{p}\right)^2I_{mi} \tag{26}$$

The active branched-chain driving force vector of the parallel manipulator is recorded as$\boldsymbol{\tau}=[F_1\quad F_2\quad F_3]^T$. Combining Eqs. (24), (25) and (26), the dynamic model of the parallel manipulator of the polishing robot can be rewritten as:

$$\boldsymbol{M}\dot{\boldsymbol{v}}_A+\boldsymbol{C}\boldsymbol{v}_A+\boldsymbol{G}+\boldsymbol{\tau}_f+\boldsymbol{E}=\boldsymbol{S}\boldsymbol{\tau} \tag{27}$$

$$\begin{cases}\boldsymbol{M}=\boldsymbol{M}_{\mathrm{m}}+\sum_{i=1}^{3}\left[\boldsymbol{e}_{4\times}\boldsymbol{a}_{i\times}+(l_4-l_{\mathrm{m}})\boldsymbol{e}_{4\times}^2\right]\boldsymbol{M}_i+\boldsymbol{S}\boldsymbol{M}_s\boldsymbol{J}\\ \boldsymbol{C}=\boldsymbol{C}_{\mathrm{m}}+\sum_{i=1}^{3}\left[\boldsymbol{e}_{4\times}\boldsymbol{a}_{i\times}+(l_4-l_{\mathrm{m}})\boldsymbol{e}_{4\times}^2\right]\boldsymbol{C}_i+\boldsymbol{S}\boldsymbol{M}_s\dot{\boldsymbol{J}}\\ \boldsymbol{G}=\boldsymbol{G}_{\mathrm{m}}+\sum_{i=1}^{3}\left[\boldsymbol{e}_{4\times}\boldsymbol{a}_{i\times}+(l_4-l_{\mathrm{m}})\boldsymbol{e}_{4\times}^2\right]\boldsymbol{G}_i\\ \boldsymbol{\tau}_f=\boldsymbol{\tau}_{f\mathrm{m}}+\sum_{i=1}^{3}\left[\boldsymbol{e}_{4\times}\boldsymbol{a}_{i\times}+(l_4-l_{\mathrm{m}})\boldsymbol{e}_{4\times}^2\right]\boldsymbol{\tau}_{fi}\\ \boldsymbol{S}=\left[\boldsymbol{e}_{4\times}\boldsymbol{a}_{1\times}\boldsymbol{e}_1+(l_4-l_{\mathrm{m}})\boldsymbol{e}_{4\times}^2\boldsymbol{e}_1,\boldsymbol{e}_{4\times}\boldsymbol{a}_{2\times}\boldsymbol{e}_2+(l_4-l_{\mathrm{m}})\boldsymbol{e}_{4\times}^2\boldsymbol{e}_2,\boldsymbol{e}_{4\times}\boldsymbol{a}_{3\times}\boldsymbol{e}_3+(l_4-l_{\mathrm{m}})\boldsymbol{e}_{4\times}^2\boldsymbol{e}_3\right]\end{cases}$$

Eq. (27) is the explicit dynamic model of the parallel manipulator for the polishing robot with the joint friction. $\boldsymbol{M}$ is the inertia matrix of the parallel manipulator of the polishing robot and its value is only related to the attitude parameters of the parallel manipulator and $\boldsymbol{M}_s=diag[M_{si}]$. $\boldsymbol{C}$ is the coefficient matrix of the centrifugal force and Coriolis force of the parallel manipulator, and its value is not only related to the attitude parameters but also related to the motion parameters. $\boldsymbol{G}$ is the gravity matrix of the parallel manipulator. $\boldsymbol{\tau}_f$ is the matrix containing the friction effects of the branched-chain joints. $\boldsymbol{E}$ is the external load matrix and $\boldsymbol{E}=\boldsymbol{E}_{\mathrm{m}}$.

4.2. Friction model of polishing robot

The motion joints of the polishing robot mainly include spherical joints, universal joints, ball screws and linear slides. UPS branched-chains are the driving components of the polishing robot, and the friction effects of its spherical joints, universal joints and ball screws are the main proportion for the dynamic model. In order to simplify the joint friction model, only the friction forces or

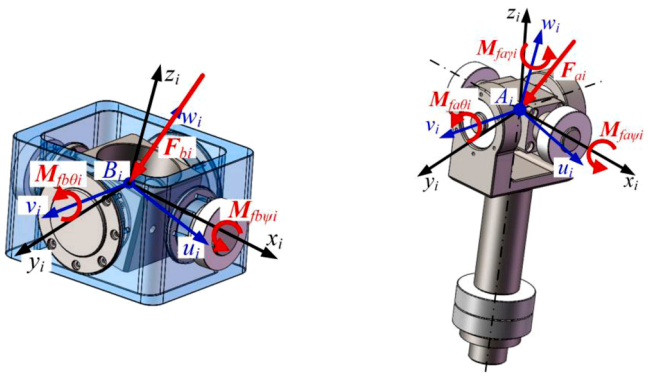

(a) **(b)**

Fig. 5. Motion joints of UPS branched-chain: (a) universal joint, (b) spherical joint.

Table 1
Structural parameters of polishing robot.

Parameter (mm)	Value	Parameter (mm)	Value
Circumcircle radius of spherical joints (a)	150.00	Length from centroid of cylinder block to B_i (l_{tv2})	125.49
Circumcircle radius of universal joints (b)	400.00	Length from centroid of UP branched-chain to its front end (l_{c1})	820.02
Length from centroid of telescopic rod to A_i (l_{r1})	657.08	Length from centroid of UP branched-chain to A (l_{m})	70.00
Length of telescopic rod (l_r)	1289.00	Ball screw lead (p)	6.00

friction moments of UPS branched-chain joints are considered, while the other motion joints are treated as ideal joints. In addition, the conventional spherical joint is replaced by a composite spherical joint for UPS branched-chains to increase the range of motion allowed and improve the bearing capacity. The composite spherical joint is composed of three pairs of vertical intersecting angular contact bearings, and the universal joint consists of two pairs of vertical intersecting angular contact bearings. The structure and force analysis of the universal joint and composite spherical joint are shown in Fig. 5.

According to Eqs. (11), (12), (13) and (14), the Newton-Euler equation of UPS branched-chain can be established, and the joint forces $\boldsymbol{F}_{ai}$ and $\boldsymbol{F}_{bi}$ can be solved. During the robot polishing operation, the friction between the ball and the inner and outer rings of the bearing will affect the driving forces of the branched-chains. In this paper, a simplified peg-hole model is used to describe the bearing friction, and the friction moment of the spherical joints and universal joints of UPS branched-chains is described by Coulomb-viscous friction model. In the joint conjoined coordinate systems $\{B_i\text{-}u_iv_iw_i\}$ and $\{A_i\text{-}u_iv_iw_i\}$, the joint friction moments can be expressed as:

$$\begin{cases} \boldsymbol{M}_{fbi}^{b} = [\,M_{fb\psi i} \quad M_{fb\theta i} \quad 0\,]^T \\ \boldsymbol{M}_{fai}^{a} = [\,M_{fa\psi i} \quad M_{fa\theta i} \quad M_{fa\gamma i}\,]^T \end{cases} \tag{28}$$

$$\begin{cases} M_{fb\psi i} = R_{bx}\left[\mu_{vh}\omega_{bxi}R_{bx} + \dfrac{\omega_{bxi}}{\|\boldsymbol{\omega}_{bi}\|}\mu_{ch}\|\boldsymbol{F}_{bi}\|\right] \\ M_{fb\theta i} = R_{bv}\left[\mu_{vh}\omega_{bvi}R_{bv} + \dfrac{\omega_{bvi}}{\|\boldsymbol{\omega}_{bi}\|}\mu_{ch}\|\boldsymbol{F}_{bi}\|\right] \end{cases}, \begin{cases} M_{fa\psi i} = R_{ax}\left[\mu_{vs}\omega_{axi}R_{ax} + \dfrac{\omega_{axi}}{\|\boldsymbol{\omega}_{ai}\|}\mu_{cs}\|\boldsymbol{F}_{ai}\|\right] \\ M_{fa\theta i} = R_{av}\left[\mu_{vs}\omega_{avi}R_{av} + \dfrac{\omega_{avi}}{\|\boldsymbol{\omega}_{ai}\|}\mu_{cs}\|\boldsymbol{F}_{ai}\|\right] \\ M_{fa\gamma i} = R_{aw}\left[\mu_{vs}\omega_{awi}R_{aw} + \dfrac{\omega_{awi}}{\|\boldsymbol{\omega}_{ai}\|}\mu_{cs}\|\boldsymbol{F}_{ai}\|\right] \end{cases} \tag{29}$$

where μ_{vh} and μ_{vs} are the viscous friction coefficients, μ_{ch} and μ_{cs} are the Coulomb friction coefficients, R_{bx} and R_{bv} are the radii of the friction circle for the bearings in the universal joint, R_{ax}, R_{av} and R_{aw} are the radii of the friction circle for the bearings in the spherical joint, $\boldsymbol{\omega}_{bi}$ and $\boldsymbol{\omega}_{ai}$ are the vectors of $\boldsymbol{\omega}_i$ in the joint reference coordinate systems, and ω_{bji} and ω_{aji} (j=x, v, w) are the three motion components of $\boldsymbol{\omega}_{bi}$ and $\boldsymbol{\omega}_{ai}$.

The friction force of the ball screw of UPS branched-chains based on Coulomb-viscous friction model can be expressed as:

$$\boldsymbol{F}_{fsi} = \left[\mu_{vb}\dot{l}_i + \mu_{cb}\|\boldsymbol{F}_{ci}^{\mathrm{n}}\|\mathrm{sgn}\left(\dot{l}_i\right)\right]\boldsymbol{e}_i \tag{30}$$

where μ_{vb} and μ_{cb} are the viscous friction coefficient and the Coulomb friction coefficient for the ball screw, and $\mathrm{sgn}(\cdot)$ is the sign function (if $\dot{l}_i > 0$, $\mathrm{sgn}(\dot{l}_i) = 1$, if $\dot{l}_i = 0$, $\mathrm{sgn}(\dot{l}_i) = 0$ and if $\dot{l}_i < 0$, $\mathrm{sgn}(\dot{l}_i) = -1$).

Table 2
Mass parameters of polishing robot

Parameter (kg)	Value
Mass of UPS branched-chain telescopic rod component (m_l)	29.19
Mass of UPS branched-chain cylinder block (m_u)	70.80
Mass of moving platform (m)	32.66
Mass of UP branched-chain (m_c)	117.83

Table 3
Inertia parameters of polishing robot.

Parameter (kg•mm^2)	Value
Inertia matrix of telescopic rod component (I_{li})	diag[5942980, 5942846, 29240]
Inertia matrix of UP branched-chain (I_c)	diag[33926032, 33944719, 628686]
Inertia matrix of moving platform (I_m)	diag[220578, 220579, 345594]
Inertia matrix of cylinder block component (I_{ui})	diag[14263739, 14597782, 203094]
Rotational inertia of driving component (I_{mi})	782

Table 4
Joint friction parameters of polishing robot.

Parameter (mm)	Value	Parameter	Value
Friction circle radius of spherical joint (R_{ax})	10.00	Coulomb friction coefficient of spherical/universal joint (μ_{ch}, μ_{cs})	0.05
Friction circle radius of spherical joint (R_{av})	8.50	Viscous friction coefficient of spherical/universal joint (N.s/m) (μ_{vh}, μ_{vs})	0.02
Friction circle radius of spherical joint (R_{aw})	15.00	Coulomb friction coefficient of ball screw (μ_{cb})	0.05
Friction circle radius of universal joint (R_{bx}, R_{bv})	25.00	Viscous friction coefficient of ball screw (N.s/m) (μ_{vb})	0.02

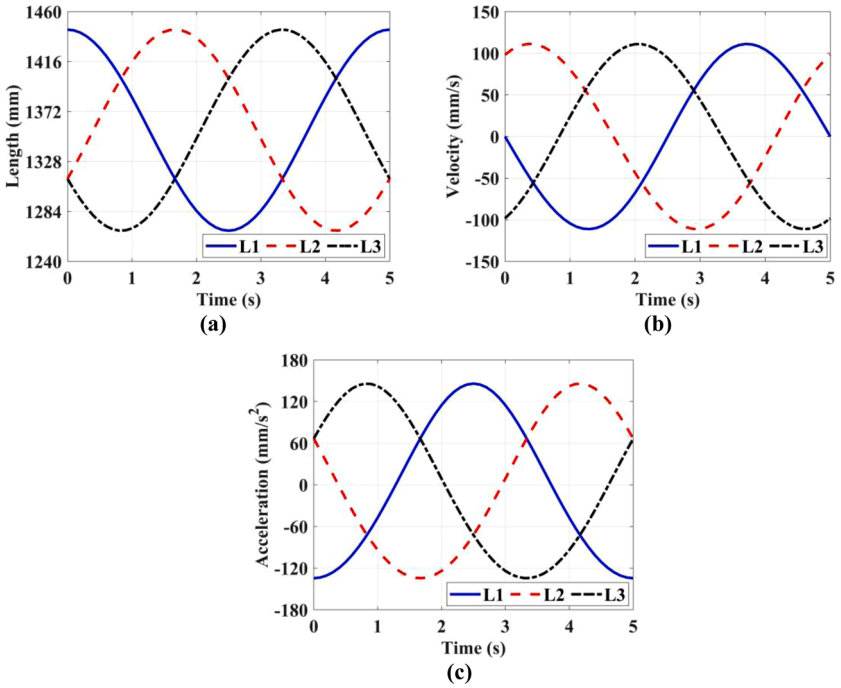

Fig. 6. Kinematic parameters of branched-chains: (a) axial length, (b) axial velocity, (c) axial acceleration.

4.3. Dynamic simulation

It is assumed that each component of the parallel manipulator is a rigid body with regular shape and uniform mass. The parameters of the parallel manipulator of the polishing robot are shown in Table 1-4.

In order to analyze the variation law of active branched-chains driving forces and inertia coupling properties of the polishing robot

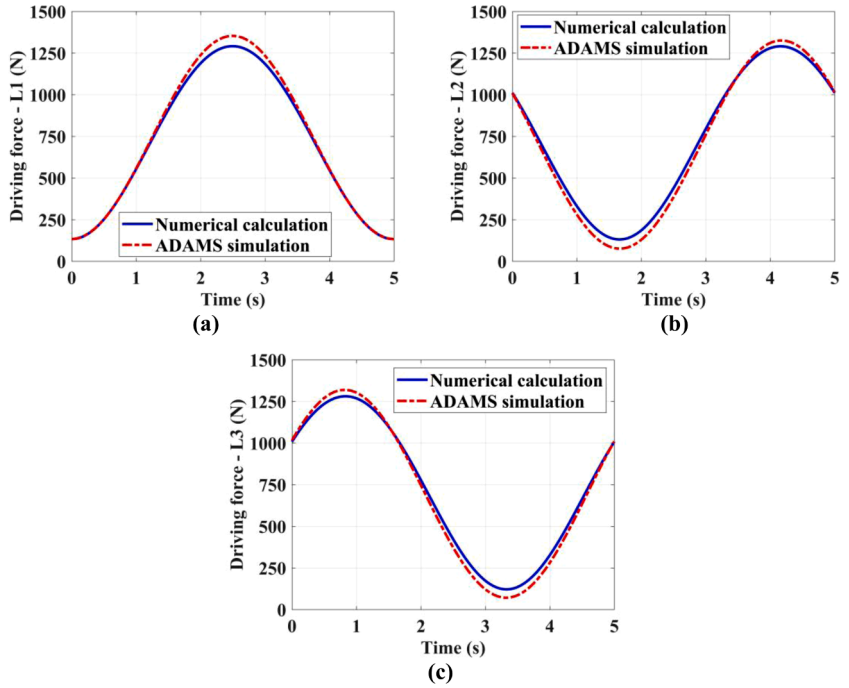

Fig. 7. Driving forces of active branched-chains of polishing robot: (a) branched-chain L1, (b) branched-chain L2, (c) branched-chain L3.

in its workspace, the circular motion in the workspace is selected for analysis. The motion trajectory of reference point *A* of the moving platform is shown in Eq. (31) and the unit is mm. Based on the kinematic model in **Section 2.2**, the axial length, velocity, and acceleration of the active branched-chains of the parallel manipulator are shown in Fig. 6, and the motion parameters of the branched-chains all show a sinusoidal trend.

$$\begin{cases} X = 300\cos(0.4\pi t) \\ Y = 300\sin(0.4\pi t) \\ Z = 1300 \end{cases} \tag{31}$$

In the dynamic model of the polishing robot, the forces and moments acting on the parallel manipulator by the serial components are treated as external loads. The parameters in Tables 1-4 are substituted into the dynamic model of the parallel manipulator, and the driving forces of active branched-chains for the polishing robot are calculated by MATLAB.

Further, the original position of the virtual prototype of the polishing robot is established with Solidworks software and imported into ADAMS software. Firstly, we add the motion joints of the robot model according to the motion characteristics of the robot components and add the joint friction coefficients in Table 4, and then we set the motion parameters of the branched-chains obtained from the kinematic model. Finally, the same simulation time as the numerical calculation is set. The driving forces of three active branched-chains based on the numerical calculation and ADAMS simulation are shown in Fig. 7.

Fig. 7 shows that the numerical calculation results of the dynamic model of the polishing robot agree with the simulation results of ADAMS when the reference point *A* of the moving platform makes a circular motion from the static platform plane at a fixed height, which indicates that the explicit dynamic model is valid. The driving forces of the active branched-chains of the parallel manipulator all show a sinusoidal function variation, with the opposite trend to the axial length of the branched-chains and the same trend to the axial acceleration. Meanwhile, the variation of the driving forces of three branched-chains has symmetry similar to the distribution of branched-chains, which further verifies the correctness of the explicit dynamic model. Besides, comparing the results of numerical calculation and ADAMS simulation, we obtain that there is only a small error for the driving force of each branched-chain. The main causes of the error are as follows: 1) The manipulator parameters used for the numerical calculation and ADAMS simulation are not completely consistent. 2) According to the error distribution of the driving force, it can be seen that the driving force error is larger when the motion direction of the branched-chain changes, which indicates that the change of the motion direction of the branched-chain has a large impact on the driving force, and the force on the branched-chain is complicated at this time.

5. Coupling property of polishing robot

5.1. Coupling evaluation index

For the robot closed-loop control system, the attitude parameters of the moving platform cannot be detected in real time, and the

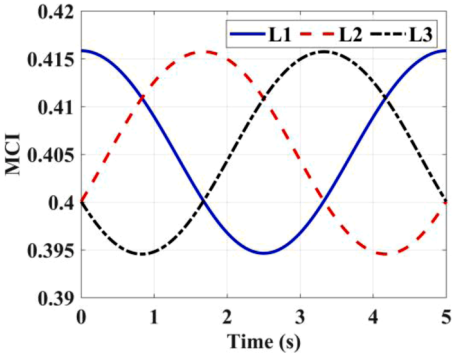

Fig. 8. Inertia coupling strength index of active branched-chains under Eq. (31).

joint control of the active branched-chain is still the main control strategy for the parallel manipulator. The three UPS branched-chains of the polishing robot need to move cooperatively to meet the attitude requirements of the grinding system in the large optical mirror polishing process. The active branched-chain of the manipulator is affected by the coupling inertia from other branched-chains in addition to the own branched-chain inertia, which will affect the dynamic properties of the polishing robot.

In order to study the coupling properties among active branched-chains of the parallel manipulator for the polishing robot, the dynamic model of the manipulator in the workspace should be transformed into the dynamic model in joint space. According to the principle that the kinetic energy of the manipulator in the generalized coordinate is equal to that in the joint space coordinate, the inertia matrix of the parallel manipulator in the joint space can be expressed as:

$$\boldsymbol{M}_{CI} = \left(\boldsymbol{J}^{-1}\right)^{T}\boldsymbol{M}\left(\boldsymbol{J}^{-1}\right) \tag{32}$$

The logarithmic function with monotonically increasing values is used to evaluate the inertia coupling strength between active branched-chains of the manipulator, and the coupling strength index MCI_i (i=1, 2, 3) of UPS branched-chain Li can be expressed as:

$$\begin{cases} \mathrm{MCI}_i = \ln(\lambda_i + 1) \\ \lambda_i = \dfrac{\sum\limits_{k=1,k\neq i}^{3} |\boldsymbol{M}_{CI}(i,k)|}{2|\boldsymbol{M}_{CI}(i,i)|} \end{cases} \tag{33}$$

The inertia matrix of the parallel manipulator has the property that the diagonal elements dominate, so that λ_i is always in the range of [0, 1]. In addition, to ensure that the coupling strength evaluation index is positive, the value of the inertia coupling strength evaluation index MCI_i of the polishing robot is defined in the interval $[0, \ln 2] \approx [0, 0.693]$. When the index is closer to ln2, the more serious the inertia coupling strength of the branched-chain Li is, and when the index is closer to zero, the less the inertia coupling strength of the branched-chain Li is.

When the coupling strength index is larger, the branched-chain of the manipulator is more affected by the inertia from other branched-chains, that is, the proportion of the coupling inertia of the branched-chain in the inertia matrix is larger. The inertia coupling strength index of each active branched-chain of the parallel manipulator under the motion trajectory of Eq. (31) is shown in Fig. 8.

Combined with Figs. 6 and 7, Fig. 8 shows that the inertia coupling strength of each active branched-chain of the parallel manipulator has an opposite trend to its driving force under the motion trajectory of Eq. (31). When the driving force of the branched-chain is larger, the length of this branched-chain is smaller, and the inertia coupling strength is also smaller. In addition, when the polishing robot moves in a circle around the center of the moving platform, the inertia coupling strength indices have the characteristic of symmetric distribution.

5.2. Coupling strength distribution in workspace

According to the structural parameters of the 5-DOF hybrid polishing robot, the following limitations are imposed on the parallel manipulator:

$$\begin{cases} l_{i\min} \le l_i \le l_{i\max} \\ |\alpha_{Ai}| \le \alpha_{\max} \\ |\beta_{Bi}| \le \beta_{\max} \end{cases} \quad (i = 1, 2, 3) \tag{34}$$

where $l_{i\min}$ and $l_{i\max}$ are the minimum and maximum allowable lengths of active branched-chains, and $l_{i\min}$=950mm, $l_{i\max}$=1770mm; α_{Ai} and β_{Bi} are the attitude angles of the spherical joint and universal joint, $\alpha_{\max}$ and $\beta_{\max}$ are the maximum allowable angles of the spherical joint and universal joint and $\alpha_{\max}=\pi/6$, $\beta_{\max}=\pi/4$.

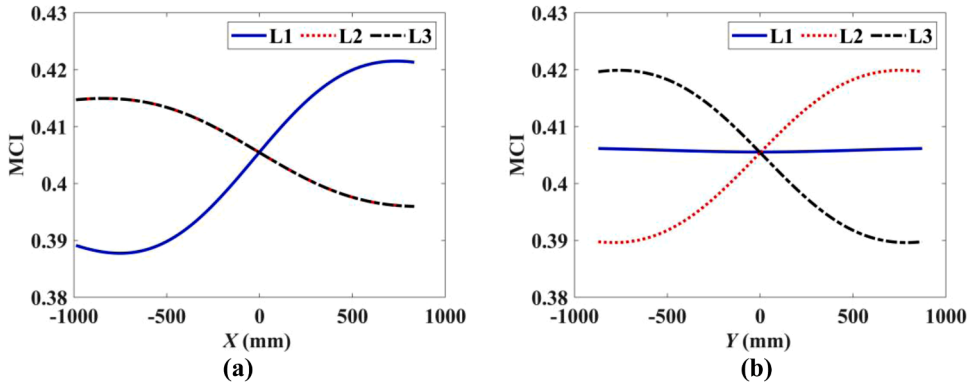

Fig. 9. Coupling strength indices of branched-chains: (a) along *X*-axis, (b) along *Y*-axis.

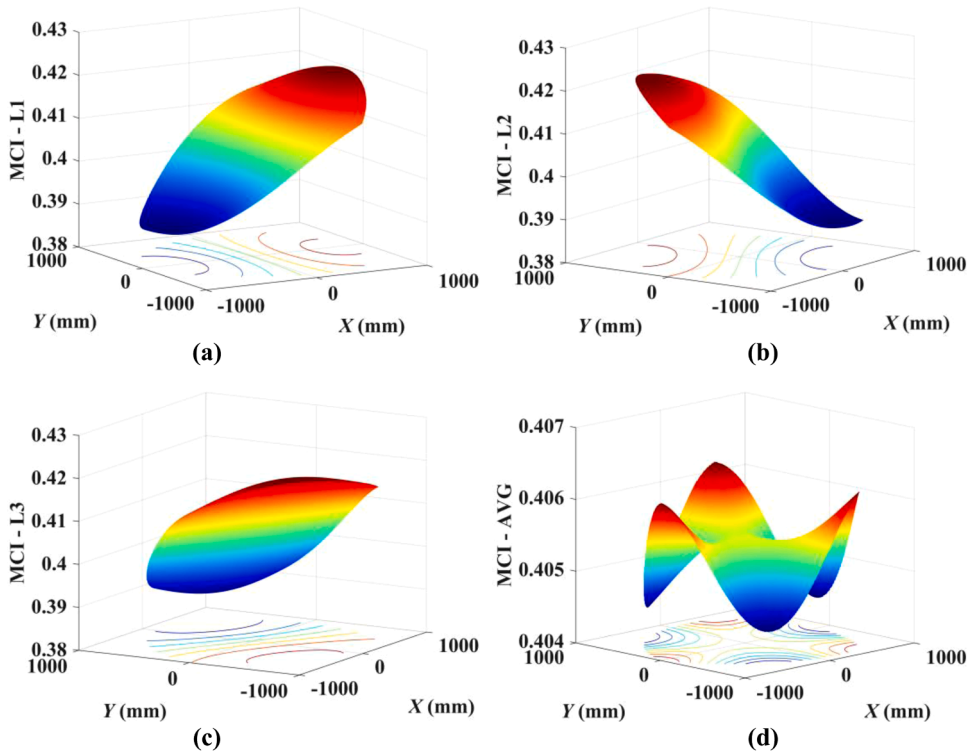

Fig. 10. Coupling strength in manipulator workspace: (a) branched-chain L1, (b) branched-chain L2, (c) branched-chain L3, (d) average value.

According to the definition of inertia coupling strength evaluation index for the active branched-chain L*i* in Eq. (33), the inertia coupling strength indices of UPS branched-chains with Z=1300mm in the base coordinate system {*B-XYZ*} are shown in Fig. 9.

Fig. 9 shows that the inertia coupling strength of each UPS branched-chain of the manipulator changes with the motion attitude of the moving platform. The inertia coupling strength indices of the branched-chains L2 and L3 have the same trend along the *X*-axis, which is consistent with the symmetric distribution of the branched-chains L2 and L3 about the X-axis. When the moving platform of the polishing robot moves along the positive direction of *X*-axis, the inertia coupling strength indices of branched-chains L2 and L3 gradually decrease, and the inertia coupling strength index of branched-chain L1 gradually increases; and the variation interval of the coupling strength indices of branched-chains L2 and L3 is smaller than that of the branched-chain L1.

The coupling strength index of the branched-chain L1 is symmetrical about $Y = 0$ mm, and the inertia coupling of branched-chain L1 from branched-chains L2 and L3 is almost constant along the *Y*-axis. The inertia coupling strengths of branched-chains L2 and L3 along the *Y*-axis have opposite trends. When the manipulator moves from the negative axis of the *Y*-axis to its positive axis, the inertia coupling strength of branched-chain L2 increases and branched-chain L3 decreases gradually.

In order to describe more intuitively the variation of inertia coupling between the active branched-chains with the motion attitude

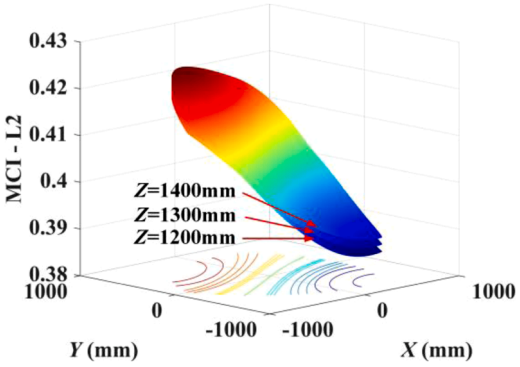

Fig. 11. Coupling strength of branched-chain L2 in different planes.

of the moving platform, the distribution of inertia coupling strength for UPS branched-chains of the polishing robot in its workspace when Z=1300mm is shown in Fig. 10.

Fig. 10 shows that the inertia coupling strength indices of UPS branched-chains in its workspace are also symmetrical. The inertia coupling strength of each active branched-chain is relatively small in the coordinate range of the branched-chain distribution. When the polishing robot moves in the direction away from one of the branched-chains, the inertia coupling strength index of this branched-chain will gradually increases, which is the same as the previous results.

The average value of the inertia coupling strength indices for active branched-chains is shown in Fig. 10(d). The average value of the coupling strength indices stays around 0.405 and varies less with the robot moves toward the workspace boundary. In addition, the average value also has a symmetric distribution characteristic in the manipulator workspace, which is related to the fact that the structural parameters of each active branched-chain of the polishing robot are not completed axially symmetric in its conjoined coordinate system.

The distribution of the inertia coupling strength of the active branched-chains along Z-axis also affects the dynamic characteristics of the manipulator. As can be seen from Fig. 8, the inertia coupling strength of three active branched-chains for the polishing robot is similar, the coupling strength index of branched-chain L2 is analyzed in different workspace planes (Z=1200mm, Z=1300mm and Z=1400mm) and the result is shown in Fig. 11. The result shows that the inertia coupling strength of the branched-chains increases with the manipulator moving in the positive direction of Z-axis.

The hybrid polishing robot is the key equipment for large optical mirrors processing, based on the distribution law of branched-chains inertia coupling strength in the workspace, the coupling between active branched-chains is inevitable, but the task space of the polishing robot can be reasonably planned to reduce the influence of the inertia coupling. At the same time, the structural parameters of the polishing robot are also important factors affecting the inertia coupling strength between the branched-chains, and some studies on the structural parameters optimization of the polishing robot can be carried out based on this study to reduce the inertia coupling between the active branched-chains of the parallel manipulator and improve the dynamic properties of the polishing robot.

6. Conclusions

In this paper, a hybrid robot composed of a 3-DOF parallel manipulator, 2R series rotary joints and a dual rotor grinding system is proposed for polishing large optical mirrors with the advantages of high stiffness and high motion accuracy.

(1) The dynamic model of the parallel manipulator is established based on Newton-Euler method considering the friction effects of the branched-chain joints. And the explicit dynamic model of the manipulator is obtained by replacing the motion parameters with the motion parameters of the reference point of the moving platform as the intermediate variables.
(2) Comparing the numerical calculation of the dynamic model and ADAMS simulation for the parallel manipulator, the results obtained have a consistent trend, and with relatively large errors only when the motion direction of the branched-chains changes, which verifies the correctness of the explicit dynamic model.
(3) Based on the dynamic model, the evaluation model of the inertia coupling strength for active branched-chains in the joint space is established with a logarithmic function, and the results show that the inertia coupling strength of each active branched-chain gradually becomes larger when the robot moves away from its layout direction, and the inertia coupling of different branched-chains is symmetrically distributed in the workspace.

The study provides a theoretical basis for the joint controller design and structural parameter optimization of the hybrid polishing robot.

Declaration of Competing Interest

The authors declare that they have no conflicts of interest.

Acknowledgments

Financial support for this work, provided by the Priority Academic Program Development of Jiangsu Higher Education Institutions (PAPD) and the National Natural Science Foundation of China (Grant No. 91648105), is gratefully acknowledged.

References

[1] X. Yang, H.T. Liu, J.L. Xiao, et al., Continuous friction feedforward sliding mode controller for a TriMule hybrid robot, IEEE/ASME Trans. Mechatron. 23 (3) (2018) 1673–1683.
[2] S.L. Canfield, J.S. Owens, S.G. Zuccaro, Zero moment control for lead-through teach programming and process monitoring of a collaborative welding robot, J. Mech. Robot. 13 (3) (2021), 031114.
[3] P. Xu, C.F. Cheung, C. Wang, et al., Novel hybrid robot and its processes for precision polishing of freeform surfaces, Precis. Eng. 64 (2020) 53–62.
[4] H.Y. Tam, H. Cheng, An investigation of the effects of the tool path on the removal of material in polishing, J. Mater. Process. Technol. 210 (5) (2010) 807–818.
[5] K. Takizawa, A. Beaucamp, Comparison of tool feed influence in CNC polishing between a novel circular-random path and other pseudo-random paths, Opt. Express 25 (19) (2017) 22411–22424.
[6] N. Plitea, A. Szilaghyi, D. Pisla, Kinematic analysis of a new 5-DOF modular parallel robot for brachytherapy, Rob. Comput. Integr. Manuf. 31 (2015) 70–80.
[7] L. Carbonari, M. Callegari, G. Palmieri, A new class of reconfigurable parallel kinematic machines, Mech. Mach. Theory 79 (2014) 173–183.
[8] Z. Liu, X. Tang, Z. Shao, et al., Dimensional optimization of the Stewart platform based on inertia decoupling characteristic, Robotica 34 (5) (2016) 1151–1167.
[9] X.L. Shan, G. Cheng, Structural error and friction compensation control of a 2(3PUS+S) parallel manipulator, Mech. Mach. Theory 124 (2018) 92–103.
[10] Y. Oba, Y. Kakinuma, Simultaneous tool posture and polishing force control of unknown curved surface using serial-parallel mechanism polishing machine, Precis. Eng. 49 (2017) 24–32.
[11] P. Xu, C.F. Cheung, B. Li, et al., Kinematics analysis of a hybrid manipulator for computer controlled ultra-precision freeform polishing, Rob. Comput. Integr. Manuf. 44 (2017) 44–56.
[12] P. Xu, C.F. Cheung, B. Li, et al., Design, dynamic analysis, and experimental evaluation of a hybrid parallel-serial polishing machine with decoupled motions, J. Mech. Robot. 13 (6) (2021), 061008.
[13] Y. Jiang, T.M. Li, L.P. Wang, Dynamic modeling and redundant force optimization of a 2-DOF parallel kinematic machine with kinematic redundancy, Rob. Comput. Integr. Manuf. 32 (2015) 1–10.
[14] G. Wu, S. Caro, S. Bai, et al., Dynamic modeling and design optimization of a 3-DOF spherical parallel manipulator, Rob. Autom. Syst. 62 (10) (2014) 1377–1386.
[15] B. Hu, J. Yu, Unified solving inverse dynamics of 6-DOF serial-parallel manipulators, Appl. Math. Modell. 39 (16) (2015) 4715–4732.
[16] J.G. Liu, Y.M. Li, Y. Zhang, et al., Dynamics and control of a parallel mechanism for active vibration isolation in space station, Nonlinear Dyn. 76 (3) (2014) 1737–1751.
[17] N. Farhat, V. Mata, A. Page, et al., Dynamic simulation of a parallel robot: Coulomb friction and stick-slip in robot joints, Robotica 28 (1) (2010) 35–45.
[18] X.C. Zhang, X.M. Zhang, Z. Chen, Dynamic analysis of a 3-RRR parallel mechanism with multiple clearance joints, Mech. Mach. Theory 78 (78) (2014) 105–115.
[19] W. Khalil, S. Guegan, Inverse and direct dynamic modeling of Gough-Stewart robots, IEEE Trans. Rob. 20 (3) (2004) 754–761.
[20] X.L. Shan, G. Cheng, Explicit dynamic modeling of a 3SPS+1PS parallel manipulator with joint friction, J. Mech. Eng. 53 (1) (2017) 28–35.
[21] G.Q. Gao, J. Wen, X.J. Liu, et al., Synchronous smooth sliding mode control for parallel mechanism based on coupling analysis, Int. J. Adv. Rob. Syst. 10 (2) (2013) 1–9.
[22] X.B. Chu, F. Gao, Kinematic coupling complexity of heavy payload forging manipulator, Robotica 30 (3) (2012) 551–558.
[23] D. Liang, Y.M. Song, T. Sun, et al., Rigid-flexible coupling dynamic modeling and investigation of a redundantly actuated parallel manipulator with multiple actuation modes, J. Sound Vib. 403 (2017) 129–151.
[24] Z.F. Shao, X.Q. Tang, X. Chen, et al., Research on the inertia matching of the Stewart parallel manipulator, Rob. Comput. Integr. Manuf. 28 (6) (2012) 649–659.
[25] Z.H. Liu, X.Q. Tang, Z.F. Shao, et al., Dimensional optimization of the Stewart platform based on inertia decoupling characteristic, Robotica 34 (5) (2016) 1151–1167.
[26] Y.B. Li, H. Zheng, P. Sun, et al., Dynamic modeling with joint friction and research on the inertia coupling property of a 5-PSS/UPU parallel manipulator, J. Mech. Eng. 55 (3) (2019) 43–52.